



Enhanced catalytic reduction of nitrophenols by sodium borohydride over highly recyclable Au@graphitic carbon nitride nanocomposites

Thanh Binh Nguyen^a, C.P. Huang^b, Ruey-an Doong^{a,c,*}

^a 101, Sec 2, Kuang Fu Road, Department of Biomedical Engineering and Environmental Sciences, National Tsing Hua University, Hsinchu, 30013, Taiwan

^b Department of Civil and Environmental Engineering, University of Delaware, Newark, 19716, DE, USA

^c 1001, University Road, Institute of Environmental Engineering, National Chiao Tung University, Hsinchu, 30010, Taiwan

ARTICLE INFO

Keywords:

Graphitic carbon nitride (g-C₃N₄) nanosheet
Au nanoparticles
Nitrophenols
Enhanced recyclable reduction
Heterostructures

ABSTRACT

In this study, a photochemical green synthesis using thermal exfoliation process is developed to fabricate Au@graphitic carbon nitride (g-C₃N₄) nanocomposite, highly recyclable and reusable, for the catalytic reduction of nitrophenols by NaBH₄. Au nanoparticles (Au NPs) in the diameter of 5–15 nm are deposited onto the surface of g-C₃N₄ in 3–6 layers of structure. The synthesized Au@g-C₃N₄ nanocomposites exhibit excellent catalytic activity and stability in the reduction of nitrophenols including 2-nitrophenol, 3-nitrophenol, 4-nitrophenol, 2,4-nitrophenol, and 2,4,6-nitrophenol. The catalytic performance of Au@g-C₃N₄ is highly dependent on the initial nitrophenol concentration, Au loading, inorganic anions, and pH. The rate constant of 4-nitrophenol reduction over Au@g-C₃N₄ (2 wt%) is 26.4 times that of pure Au NP in the presence of 7 mM of NaBH₄ at pH 5. Moreover, Au@g-C₃N₄ can be reused for at least 10 consecutive cycles without considerable loss of catalytic activity. The presence of anions (0.1 M) such as H₂PO₄[−], SO₄^{2−}, HCO₃[−], and NO₃[−] decreases the rate of 4-nitrophenol reduction by a factor of 1.2–8.8; whereas there is a 1.2-time increase in rate constant upon the addition of Cl[−] ion. The detection of H[•] radical adducts indicates that Au NPs adsorb BH₄[−] ions and forms Au-H species. The porous and conductive g-C₃N₄ provides large surface area for nitroarene adsorption and subsequent electron transfer from the Au-H species to 4-nitrophenol, which results in accelerating the reduction of 4-nitrophenol. Results clearly demonstrate that Au@g-C₃N₄ is a promising green catalyst of enormous potential for nitroaromatic reduction, which provides a new venue for tailoring Au-based nanomaterials in elucidation of a wide variety of heterogeneous catalytic reactions.

1. Introduction

Noble metal based nanomaterials have recently attracted considerable attention because of their unique physicochemical properties and great potentials in diverse fields such as optical, catalytic, biomedical, petrochemical and environmental applications [1–3]. Gold nanoparticle (Au NP) is one of the most promising nanomaterials, which plays an important role in catalytic processes including low-temperature CO oxidation [4], reductive catalysis of chlorinated and nitrogenated aromatics [5], and organic synthesis [6]. In particular, the reduction of 4-nitrophenol (4-NP) to 4-aminophenol, an important manufacture intermediate of analgesic and antipyretic drug [7], over Au NPs in the presence of reducing agent such as NaBH₄ and hydrogen gas has been extensively investigated [1,5,7,8]. However, Au NPs are easily agglomerated because of high surface energy, which

subsequently lead to rapid decrease in catalytic activity and poor durability. Therefore, the improvement of the catalytic efficiency and longevity of Au NPs has become the focus of research on practical applications.

Several studies have reported the possibility of using solid supports such as polymers [9], carbonaceous materials [10], and metal oxides [11] on which Au NPs is homogeneously dispersed that enhances the catalytic activity and reduces the cost of Au-based nanocatalysts. Two-dimensional (2D) materials have recently attracted considerable interest because of high surface area, appropriate chemical anchoring sites, and thermal stability [12]. Among these materials, graphitic carbon nitride (g-C₃N₄), an organic polymeric semiconductor mainly consisting of carbon and nitrogen with a band gap of 2.7 eV, exhibits high thermal and chemical stability, excellent electron transfer ability, and easy recycling [13], and has been commonly used as a

* Corresponding author at: 101, Sec 2, Kuang Fu Road, Department of Biomedical Engineering and Environmental Sciences, National Tsing Hua University, Hsinchu, 30013, Taiwan.

E-mail addresses: huang@udel.edu (C.P. Huang), radoong@mx.nthu.edu.tw (R.-a. Doong).

<https://doi.org/10.1016/j.apcatb.2018.08.035>

Received 24 February 2018; Received in revised form 8 August 2018; Accepted 15 August 2018

Available online 22 August 2018

0926-3373/ © 2018 Elsevier B.V. All rights reserved.

photocatalyst for the effective decomposition of various hazardous chemicals. Furthermore, $g\text{-C}_3\text{N}_4$ has been successfully utilized as a support to disperse and stabilize metal nanoparticles such as Pd [14], Pt [15], Cu [16], and Co [17]. Basically, $g\text{-C}_3\text{N}_4$ is formed by the linkage of N bridged tri-s-triazine repeating unit, which is generated by two-dimensional conjugated planes packed together via van der Waals interactions. In view of its unique structure and preponderance, $g\text{-C}_3\text{N}_4$ has been widely employed in a wide variety of fields such as oxygen reduction reaction [18], photocatalysis [19], photoelectrochemical reaction [20], and sensor [21]. Recently, Cai et al. have reported that the hydrophobic $g\text{-C}_3\text{N}_4$ nanosheets can be an excellent adsorbent for the removal of metal ions and organic compounds [22]. For heterogeneous catalytic processes, organic compounds and metal derivatives could bind or intercalate into the matrix of $g\text{-C}_3\text{N}_4$ through the surface anchoring sites to improve the catalytic reaction rate, and thus broaden the catalytic application of $g\text{-C}_3\text{N}_4$ toward organic decomposition. The unique architecture of $g\text{-C}_3\text{N}_4$ and the outstanding catalytic performance of Au nanoparticles provide a great impetus to use $g\text{-C}_3\text{N}_4$ as a promising support to judiciously decorate Au NPs for the formation of highly active and green heterogeneous catalyst. More interestingly, structure wise, Au NPs and $g\text{-C}_3\text{N}_4$ are interdependent and mutually reinforcing. Up to now, the combination of Au NPs with $g\text{-C}_3\text{N}_4$ nanosheets as efficient nanocatalysts for the rapid decomposition of nitroarenes has received little attention. Recently, Fu et al. studied the reduction of p-nitrophenol over $\text{Au}@g\text{-C}_3\text{N}_4$ by NaBH_4 under dark and light irradiation and reported that $\text{Au}@g\text{-C}_3\text{N}_4$ was much efficient in degrading p-nitrophenol compared to pure Au nanoparticles [23]. However, factors such as catalyst dosage, type of nitro-phenol, initial nitrophenol concentration, pH, and temperature, affecting the reduction rate and most importantly, the mechanism regarding the reduction of nitrophenols remains little explored. Furthermore, it is expected that the synthesis procedures, i.e., precursors and processes can also affect the catalysis reactivity. This has prompted us to explore the catalytic performance $\text{Au}@g\text{-C}_3\text{N}_4$ catalyst and the mechanism of the reduction of nitroaromatics by NaBH_4 over this catalyst. It is expected that results will benefit the advances of both industrial wastewater treatment processes and green technology development.

Herein, a simple fabrication method using photodeposition procedure for the synthesis of $\text{Au}@g\text{-C}_3\text{N}_4$ nanocatalysts is developed. The $\text{Au}@g\text{-C}_3\text{N}_4$ nanocomposites are then used for the catalytic reduction of nitroaromatic compounds including 2-nitrophenol (2-NP), 3-nitrophenol (3-NP), 4-nitrophenol (4-NP), 2,4-dinitrophenol (2,4-DNP), and 2,4,6-trinitrophenol (2,4,6-TNP) in the presence of NaBH_4 . Scheme 1 shows the preparation of $\text{Au}@g\text{-C}_3\text{N}_4$ by photoreduction and the catalytic degradation of nitrophenols. The Au NPs on the $g\text{-C}_3\text{N}_4$ nanosheets can be generated by photoreduction in the presence of 0.5–3 wt% Au under 365-nm UV light. The content of Au is controlled by the added amount of Au precursor. The catalytic activity and stability of $\text{Au}@g\text{-C}_3\text{N}_4$ nanocatalysts toward nitrophenols reduction is examined. In addition, the effect of NaBH_4 concentration, Au content, inorganic anions, and pH on the reaction kinetics is examined. Results show that 5–15 nm Au NPs are deposited onto $g\text{-C}_3\text{N}_4$ in 3–6 layers of nanosheets and can be recycled for at least 10 times to completely reduce nitrophenols. The detection of H^\bullet radical adducts indicates the occurrence of H abstract reaction from the Au NP and the possible mechanism for the enhanced conversion efficiency of nitrophenols by $\text{Au}@g\text{-C}_3\text{N}_4$ is proposed.

2. Experimental

2.1. Synthesis of $g\text{-C}_3\text{N}_4$

The $g\text{-C}_3\text{N}_4$ nanosheet is synthesized via the thermal exfoliation of bulk $g\text{-C}_3\text{N}_4$. Bulk $g\text{-C}_3\text{N}_4$ powder is first prepared using a modified thermal oxidation etching method by heating 10 g of thiourea in a covered alumina crucible in a muffle furnace at 550 °C for 2 h at a rate

of 15 °C min^{−1}. The yellow powder product is then well-milled in an agate mortar after cooling naturally to room temperature. The ground bulk $g\text{-C}_3\text{N}_4$ is again heated at 550 °C for 2 h in air at a rate of 15 °C min^{−1}. Finally, a pale yellow powder consisting of $g\text{-C}_3\text{N}_4$ nanosheets is obtained.

2.2. Synthesis of $\text{Au}@g\text{-C}_3\text{N}_4$

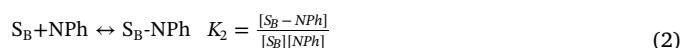
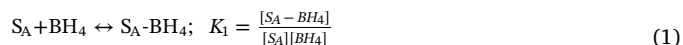
$\text{Au}@g\text{-C}_3\text{N}_4$ nanocatalyst is synthesized by the photodeposition method. Generally, 0.5 g of the as-prepared $g\text{-C}_3\text{N}_4$ nanosheets are dispersed in 100 mL of deionized water (18.2 MΩ-cm) and ultrasonicated to obtain the homogeneous dispersion. HAuCl_4 (0.25–1.5 mL of 10 mg-Au mL^{−1}) aqueous solutions (corresponding to 0.5–3.0 wt% Au) are then added into the above suspension dropwise under vigorous stirring for 30 min at room temperature. The Au NPs are deposited onto the $g\text{-C}_3\text{N}_4$ by the photo-reduction of Au(III) under the irradiation of an UV lamp, 365-nm at 64 W, for 3 h and constant stirring. Isopropanol (0.1 mL) is also added into the solution as hole scavenger. The resultant nanocomposite is separated by centrifugation and washed with deionized water several times. Finally, the $\text{Au}@g\text{-C}_3\text{N}_4$ nanocatalyst is obtained by drying at 80 °C overnight in a vacuum oven. Besides, pure Au NPs are also synthesized following the same procedures as above except without the addition of $g\text{-C}_3\text{N}_4$ nanosheets. The transmission electron microscopy (TEM) image shows that the mean diameter of the as-prepared Au NPs is 18 nm (Fig. S1, Supplementary data) after the irradiation of UV light at 365-nm for 3 h.

2.3. Catalytic reduction of nitrophenols

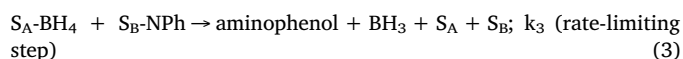
The catalytic activity of $\text{Au}@g\text{-C}_3\text{N}_4$ nanocomposite is examined by the reduction of nitrophenols in the presence of NaBH_4 . Forty μL of 10 mM nitrophenols, including 2-NP, 3-NP, 4-NP, 2,4-DNP, and 2,4,6-TNP, and 0.04–0.16 mL of 0.1 M NaBH_4 are added into 2 mL of deionized water. The well-mixing solutions are introduced into a 3-mL quartz cuvette followed by the addition of 2 mg of $\text{Au}@g\text{-C}_3\text{N}_4$ nanocatalyst to the mixture. The color of mixture changes rapidly from yellow to colorless as the reaction proceeds and the change in absorption spectra in the solution is monitored at a regular time interval of 1 min by UV–visible spectrophotometer (U4100, Hitachi, Tokyo, Japan).

2.4. Reaction kinetics

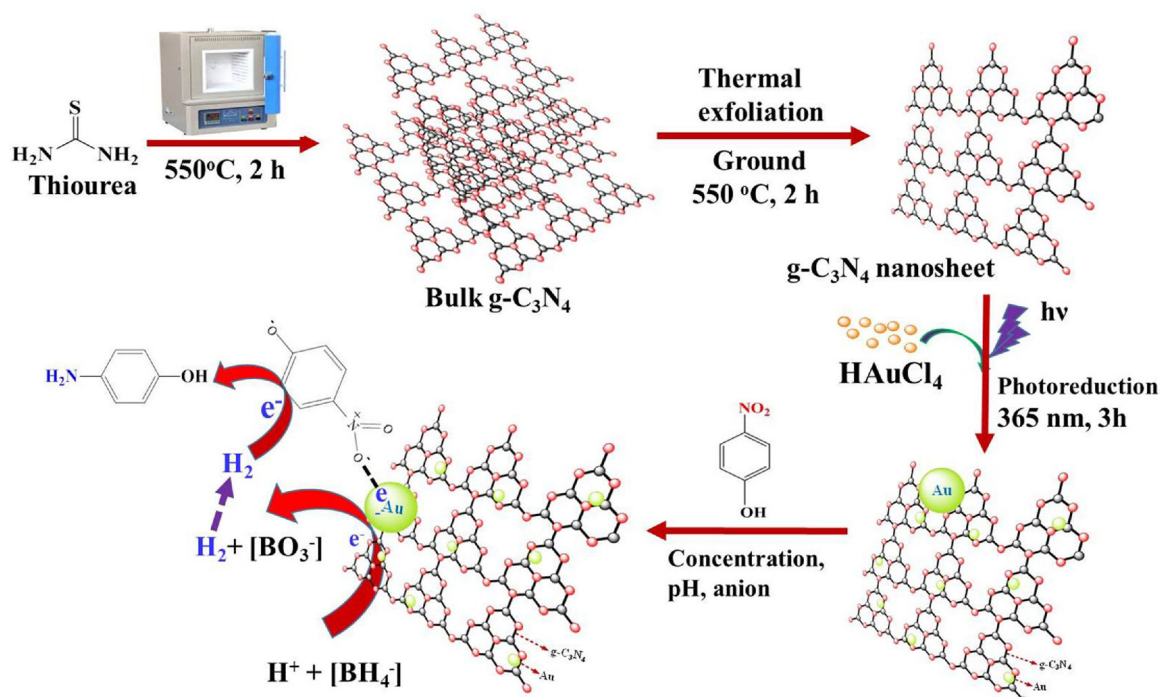
According to the Langmuir-Hinshelwood kinetics of heterogeneous catalysis, adsorption of reactants onto the catalyst surface is the first reaction step. Lin and Doong [5] have reported the reduction of nitroaromatic compounds by NaBH_4 over Au surface. Assuming that at the onset of the reaction, BH_4^- adsorbs onto the active Au site, S_A , to form surface-hydrogen species [24], and nitrophenols (NPh) adsorbs onto the different active $g\text{-C}_3\text{N}_4$ site, S_B of the $\text{Au}@g\text{-C}_3\text{N}_4$ nanocomposites rapidly, according to the following equilibrium reactions:



where K_1 and K_2 are the adsorption equilibrium constants of BH_4^- and NPh on the different active sites of Au NPs, respectively. $S_A\text{-BH}_4$ and $S_B\text{-NPh}$ are the adsorbed BH_4^- and NPh species on the $\text{Au}@g\text{-C}_3\text{N}_4$ surface, respectively. The reaction between the adsorbed nitrophenols and borohydride is the rate-limiting step, that is,



From Eq. (3), one has the rate expression:



Scheme 1. Schematic illustration of the fabrication procedure of Au@g-C₃N₄ nanocomposites.

$$\text{rate}(r) = \frac{d[\text{NPh}]}{dt} = k_3 [\text{S}_A - \text{BH}_4] \left[\text{S}_B - \text{NPh} \right] \quad (4)$$

where k_3 is the reaction rate constant. From Eqs. (1) and (2), one has:

$$[\text{S}_A - \text{BH}_4] = K_1 [\text{S}_A] [\text{BH}_4] \quad (5)$$

and

$$[\text{S}_B - \text{NPh}] = K_2 [\text{S}_B] [\text{NPh}] \quad (6)$$

From the following mass balance relationship, one has:

$$S_A^T = [\text{S}_A] + [\text{S}_A - \text{BH}_4] \quad (7)$$

and

$$S_B^T = [\text{S}_B] + [\text{S}_B - \text{NPh}] \quad (8)$$

Combining Eqs. 5 and (7), and Eqs. (6) and (8), one has:

$$[\text{S}_A - \text{BH}_4] = \frac{S_A^T K_1 [\text{BH}_4]}{1 + K_1 [\text{BH}_4]} \quad (9)$$

and

$$[\text{S}_B - \text{NPh}] = \frac{S_B^T K_2 [\text{NPh}]}{1 + K_2 [\text{NPh}]} \quad (10)$$

By substituting Eqs. (9) and (10) into (4), the reaction rate expression is:

$$r = -\frac{d[\text{NPh}]}{dt} = k_3 \frac{S_A^T K_1 [\text{BH}_4]}{1 + K_1 [\text{BH}_4]} \frac{S_B^T K_2 [\text{NPh}]}{1 + K_2 [\text{NPh}]} \quad (11)$$

Wunder et al. [25] have investigated the catalytic activity of silver nanoparticles (Au NPs) in aqueous solution for the reduction of 4-NP by NaBH₄ and reported that the adsorption constant of BH₄[−] on Au NPs was in the range of (76 ± 11) – (87 ± 13) L mol^{−1} at 10–30 °C. Moreover, Blanco et al. [26] studied the reduction of 4-NP NaBH₄ over cucurbit[7]uril functionalized Au NPs and reported an BH₄[−] adsorption constant of 7.8 ± 0.3 L mol^{−1}. Since the NaBH₄ used in this study is at the milli-molar level, it is expected that 1 > > K₁[BH₄]. Accordingly, Eq. (11) can be simplified as:

$$r = -\frac{d[\text{NPh}]}{dt} = k_3 S_A^T S_B^T K_1 K_2 [\text{BH}_4] \frac{[\text{NPh}]}{1 + K_2 [\text{NPh}]} \quad (12)$$

Furthermore, at excess surface site density of A and B, and BH₄ concentration, Eq. (12) can be simplified as the following:

$$r = -\frac{d[\text{NPh}]}{dt} = k_{\text{obs}} [\text{NPh}] \quad (13)$$

where

$$k_{\text{obs}} = \frac{k_3 S_A^T S_B^T K_1 K_2 [\text{BH}_4]}{1 + K_2 [\text{NPh}]} \quad (14)$$

It is noted that at 4-NP concentration relatively lower than NaBH₄, or 1 >> K₂[NPh], Eq. (14) can be further simplify to $k_{\text{obs}} = k_3 S_A^T S_B^T K_1 K_2 [\text{BH}_4]$.

2.5. Characterization

The surface morphology of the as-synthesized g-C₃N₄ and Au@g-C₃N₄ is characterized by field emission scanning electron microscope (SEM, Hitachi SU8010) with an acceleration electron voltage of 15 kV. All samples are Pt-coated using Ion Sputter ε-1030 (Hitachi, Tokyo) to increase the conductivity. TEM (JEOL 2011) and high-resolution TEM (HRTEM) (FEI Tecnai G2) at the acceleration voltage of 200 and 300 kV, respectively, are used to determine the structure and morphology of the g-C₃N₄ based samples. Atomic force microscopy (AFM) images are recorded by a Bruker Bioscope system (Bruker, USA). Furthermore, electron probe microanalysis (EPMA) is utilized to characterize the distribution of Au on g-C₃N₄ using an electron probe X-ray microanalyzer (JEOL JXA-8200) with an acceleration voltage of 20 kV and a beam current of 20 nA. Powder X-ray diffraction (XRD) patterns are collected via a Bruker D8 Advance X-ray diffractometer (Bruker, USA) with Ni-filtered Cu Kα radiation (λ = 1.5406 Å) operated at a generator voltage of 40 kV and an emission current of 40 mA. The patterns are acquired over the 2θ range of 5–85° with sampling step width of 0.017° (step time = 0.5 s).

The optical spectra and catalytic activity of the Au@g-C₃N₄ are examined using a Hitachi U-4100 UV–visible spectrophotometer with

the integrating sphere accessory for diffuse reflectance spectra. The Brunauer-Emmett-Teller (BET) specific surface area and pore size distribution are determined by nitrogen adsorption and desorption at 77°K using a surface area and porosimetry system (ASAP 2020, Micromeritics). The pore size and volume of the Au@g-C₃N₄ materials are determined following Barrett, Joyner, and Halenda's (BJH) mathematical models. The thermal stability of all samples is carried out using the thermogravimetric analyzer (TGA) on a Mettler Toledo TGA/DSC 3 + STAR in the temperature range of 30–1000 °C at a rate of 10 °C min⁻¹ in N₂. Zeta potential and hydrodynamic diameter are measured by Zetasizer Nano ZS (Malvern) at 25 °C. The X-ray photoelectron spectroscopy (XPS) measurements are performed on an ESCA PHI 1600 photoelectron spectrometer from Physical Electronics using Al K α radiation with a photon energy of 1486.6 eV operated at 1×10^{-9} torr and room temperature. The high-resolution spectra are recorded with the pass energy and electron volt step of 23.5 and 0.1 eV, respectively. Furthermore, the binding energy is referenced to the carbon C 1s peak at 284.8 eV. Electron paramagnetic resonance (EPR) spectra are recorded with EPR spectrometer (Bruker, EMX-10, Germany) working at X-band frequency of 9.49–9.88 GHz with power of 8.02 mW.

3. Results and discussion

3.1. Characterization of Au@g-C₃N₄ heterostructures

The morphology as well as the particle size distribution of as-prepared g-C₃N₄ nanosheets and Au@g-C₃N₄ nanocomposites are examined. Fig. 1a shows the SEM image of the exfoliated g-C₃N₄. The typical 2-D structure interconnected with wrinkled g-C₃N₄ nanosheets is observed vividly, indicating the successful split of bulk C₃N₄ layers into small and thin nanosheets via thermal exfoliation. The AFM image displays that the g-C₃N₄ nanosheets are well-separated (Fig. 1b) with a thickness of ca. 0.7 nm (Inset of Fig. 1b), indicating the successful exfoliation of bulk g-C₃N₄ into 3–6 layers of C₃N₄ nanosheets. The TEM image (Fig. 1c) shows the lamellar structure of g-C₃N₄, which is formed by the linkage of graphitic-like planes. After loading 2 wt% of Au NPs, a homogeneous distribution of Au NPs on the g-C₃N₄ nanosheets is

clearly observed in the TEM image (Fig. 1d), depicting the successful formation of Au@g-C₃N₄ nanocomposites. The HRTEM image clearly shows the characteristic lattice fringe with crystal plane distance of 0.236 nm (Fig. 1e), which corresponds to the (111) plane of face centered cubic (fcc) Au NPs. The strong interfacial interaction between Au NP and g-C₃N₄ layer is also observed in the HRTEM image, and is conducive to the electron transfer processes. Furthermore, the particle size distribution of Au NPs on g-C₃N₄ can be calculated from the histogram analysis, and the Au NPs on the g-C₃N₄ nanosheets are in the range of 5–15 nm with a mean diameter of 8 nm (Fig. 1f). The particle size of Au NPs on g-C₃N₄ is smaller than that of Au NPs alone (18 nm), indicating that the g-C₃N₄ nanosheet is an excellent support to homogeneously disperse Au NPs that constrains the growth of Au NPs.

The distribution of Au species on the g-C₃N₄ surface is determined by EPMA. As illustrated in Fig. 2, the elemental images of Au, C, and N in Au@g-C₃N₄ nanocomposites indicate the homogeneously dispersed distribution of Au atom in Au@g-C₃N₄. The distribution of C and N images match well, depicting the successful formation of g-C₃N₄. In addition, the low intensity of Au atom in comparison with C and N atoms is mainly attributed to the low Au loading of 2 Au-wt%. It is noteworthy that the EDS spectrum exhibits high intensity signals of O, C, and N elements with several low intensity of Au peaks (Fig. S2, Supplementary data), which is in good agreement with the EPMA result. The Au content in the nanocomposites is also determined by ICP-OES and a concentration of 2 wt% is observed, which is consistent with the added amount of Au ions.

Fig. 3a shows the XRD patterns of as-prepared g-C₃N₄, Au NPs, and Au@g-C₃N₄. The Au NPs show several diffraction peaks centered at 2 θ of 38.2°, 44.6°, 64.8°, 77.6°, and 83.2°, which are the characteristic peaks of (111), (200), (220), (311) and (222) crystal facets of face-centered cubic (fcc) Au NPs, respectively (JCPDS 04-0784). Both g-C₃N₄ and Au@g-C₃N₄ exhibit two distinct peaks at 2 θ of 13.2° and 27.5°, which is in good agreement with the typical graphite-like hexagonal phase of g-C₃N₄ (JCPDS 87-1526). The most intense peak at 27.5° with a d-spacing of 0.323 nm is the (002) plane of the inter-layer stacking conjugated aromatic C₃N₄ units, while the small peak at 13.2° with a d-spacing of 0.68 nm can be indexed as the (100) plane of C₃N₄, which belongs to the in-plane structural packing motif between nitride

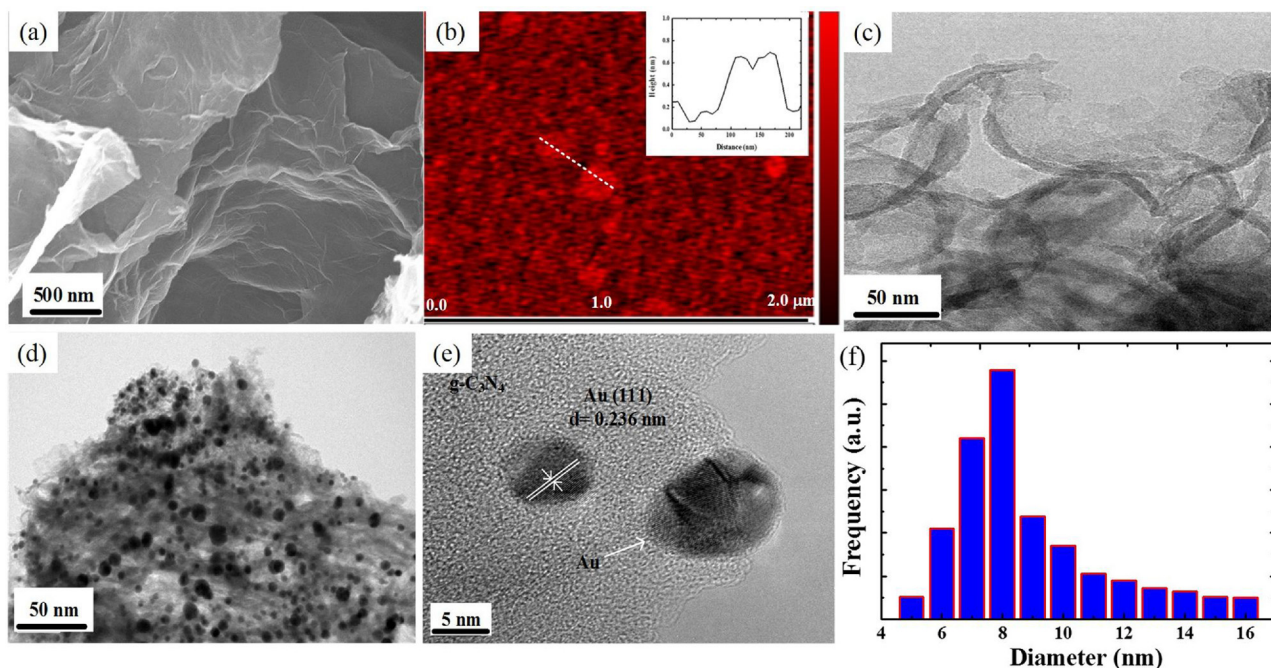


Fig. 1. (a) SEM, (b) AFM, and (c) TEM images of as-prepared g-C₃N₄ nanosheets; (d) TEM and (e) HRTEM images of Au@g-C₃N₄ nanocomposites, and (f) histogram of Au particle size distribution in Au@g-C₃N₄ nanocomposites.

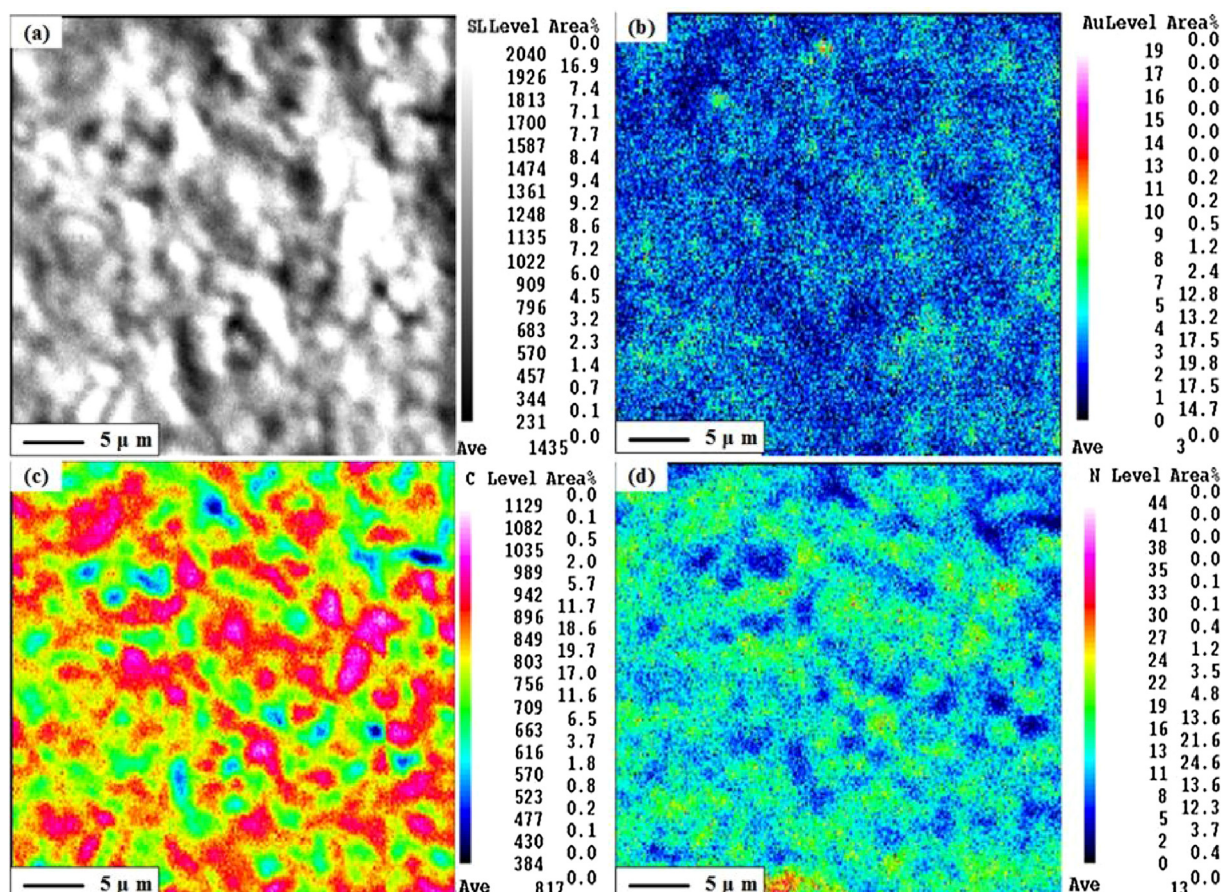


Fig. 2. (a) Backscatter SEM image of Au@g-C₃N₄ and the related EPMA elemental mapping of (b) Au, (c) C, and (d) N atoms.

pores [24]. Furthermore, the two additional weak peaks at 38.2° and 44.6° are observed when 2 wt% of Au NPs are loaded to the g-C₃N₄ nanocomposites, are assigned to the Au (111) and (200) crystal planes, respectively. The average particle size, calculated from the Au (111) peak, according to the Scherrer equation, is 8.1 nm, which is in good agreement with the TEM result.

Fig. 3b shows the UV-visible diffuse reflectance spectra of g-C₃N₄, Au NPs, and Au@g-C₃N₄ nanocomposites. It is clear that the absorption edge of g-C₃N₄ at about 450 nm is related to the characteristic absorption peak of graphite-like stacked layer structure and the π - π conjugation of C₃N₄ [25]. This absorption spectrum corresponds to the band gap of 2.76 eV, which is in good agreement with the reported data [12]. The UV-visible spectrum for Au NPs exhibits a characteristic plasmon band at 532 nm, whereas the plasmon band diminishes in the

Au@g-C₃N₄ nanocomposites because of the low Au NPs loadings. In addition, the incorporation of Au NPs on the g-C₃N₄ layers quenches the photoluminescence intensity compared with that of g-C₃N₄ (Fig. S3, Supplementary data), presumably due to the efficient separation of photogenerated charge carriers due to the electron-sink effect of Au.

Fig. S4 (Supplementary data) shows the N₂ adsorption-desorption isotherm and pore size distribution of g-C₃N₄ based nanomaterials. Both g-C₃N₄ and Au@g-C₃N₄ show typical type IV isotherm with H3-type hysteresis loop in the relative pressure range of 0.0.95, indicating the mesoporous structure nature of g-C₃N₄. In addition, g-C₃N₄ exhibits a broad pore size distribution (2–140 nm) with a two bimodal distribution (5 and 55–70 nm) after thermal oxidation process (Inset of Fig. S4), which is attributed to the random-stacking of nanosheets. The adsorption-desorption curve of Au@g-C₃N₄ also exhibits type IV isotherm and

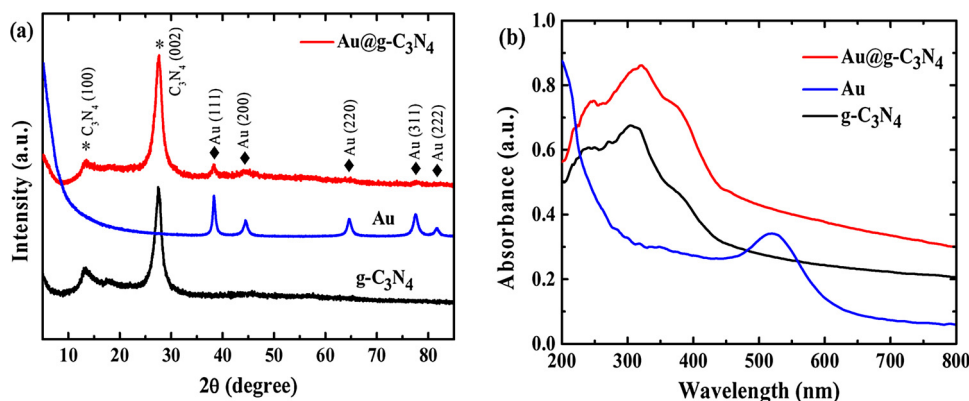


Fig. 3. (a) XRD patterns and (b) UV-visible diffused reflectance spectra of g-C₃N₄ and Au@g-C₃N₄ nanocomposites.

the specific area of Au@g-C₃N₄ is 22 m² g⁻¹, which is slightly higher than that of g-C₃N₄ (16 m² g⁻¹). It is noted that the hysteresis loop of Au@g-C₃N₄ shifts slightly to the relative pressure range of 0.5–0.9, which indicates the change in pore texture. As shown in the inset of Fig. S4 (Supplementary data), the pore size distribution of Au@g-C₃N₄ shows a main peak at approximately 2–5 nm, which is due to the deposition of Au NPs onto g-C₃N₄ surface that blocks the large mesopores of g-C₃N₄.

Fig. S5 (Supplementary data) shows the thermogravimetric profile of g-C₃N₄ and Au@g-C₃N₄ under nitrogen atmosphere. The pristine g-C₃N₄ shows the thermal stability up to 500 °C and the weight loss increases dramatically in the range of 500–700 °C. A nearly complete decomposition of g-C₃N₄ is observed at 700 °C. Addition of Au NPs enhances the thermal stability slightly and the weight of Au@g-C₃N₄ nanocomposites starts to decrease at 550 °C, which is mainly due to the strong interaction between Au NPs and the layer-stacking motif of g-C₃N₄ [26]. Furthermore, the decomposition of Au@g-C₃N₄ ends at 750 °C with a residual weight fraction of 2 wt%, which is in good agreement with the result of Au loading obtained from ICP-OES.

XPS is further used to understand the chemical composition as well as the change in chemical species of C₃N₄ before and after the addition of Au NPs. As illustrated in Fig. 4a, the full scan spectra of both g-C₃N₄ and Au@g-C₃N₄ shows C 1s and N 1s peak at 288 and 399 eV, respectively. Moreover, an additional Au 4f peak at 87 eV appears in Au@g-C₃N₄, confirming the existence of Au NPs on the surface of g-C₃N₄. After deconvolution of the C 1s spectrum (Fig. 4b), three peaks at binding energy of 284.6, 285.5, and 288.0 eV appear, which correspond to the C=C, C–N–C and C–(N)₃ bonds, respectively [27]. The N 1s spectrum also can be deconvoluted into three peaks (Fig. 4c). The main signal at 398.2 eV indicates the C–N–C in the triazine rings, whereas the other two weak peaks at 399.6 eV and 401.6 eV can be ascribed to

the bridging nitrogen atoms of N–(C)₃ and N–H, respectively [28]. The Au 4f spectra (Fig. 4d) of all Au@g-C₃N₄ catalysts are characterized by two peaks with binding energy of 83.2 and 87.4 eV for Au 4f_{7/2} and Au 4f_{5/2}, respectively, which is in good agreement with metallic Au [29]. Moreover, the peak intensity of Au 4f increases with the increase in Au content from 0.5 to 3 wt%, which is in good agreement with the added Au loading.

3.2. Effect of Au content on the catalytic activity of Au@g-C₃N₄

The catalytic performance of Au@g-C₃N₄ nanocatalysts is evaluated by the reduction of 4-NP to 4-aminophenol in the presence of NaBH₄. Fig. S6 (Supplementary data) shows the typical UV-visible spectra of 4-NP in the presence of Au@g-C₃N₄ (2 wt%) and NaBH₄. The aqueous 4-NP solution exhibits a maximum absorption peak (λ_{max}) at 317 nm originally and then red shifts to 400 nm after the addition of NaBH₄, indicating the formation of 4-nitrophenolate ions (Fig. S6a, Supplementary data) [23,30]. After the addition of 2 wt% of Au@g-C₃N₄ nanocatalysts, the peak intensity at 400 nm decreases rapidly with the concomitant increase in 4-aminophenol peak intensity at 300 nm. Besides, the initially light yellow solution becomes colorless within 10 min (Fig. S6b, Supplementary data), which means that 4-NP is almost completely reduced to 4-aminophenol. Moreover, no change in 4-NP concentration is observed after the addition of NaBH₄ in the absence of Au@g-C₃N₄ catalyst for 10 min, which is similar to that of Au NPs without the addition of NaBH₄ (Fig. S7, Supplementary data).

Fig. 5 shows the mass loading effect of Au NPs in Au@g-C₃N₄ on the catalytic reduction efficiency of 4-NP in the presence of 7 mM NaBH₄. It is clear that g-C₃N₄ is catalytically inactive on the reduction of 4-NP. Although the reaction of 4-NP ($E^{\circ}_{(4\text{-NP}/4\text{-AP})} = -0.76$ V) with NaBH₄ ($= -1.33$ V) is thermodynamically favorable, the reduction of 4-NP by

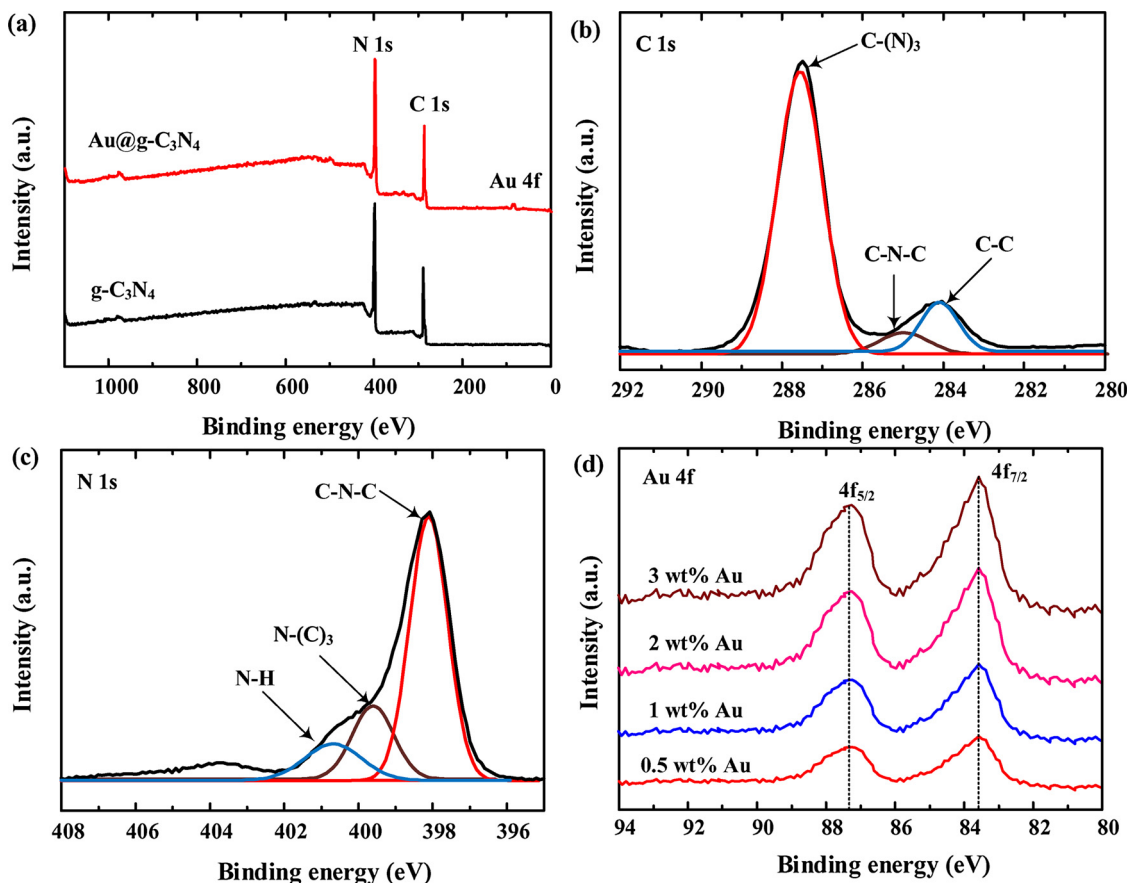


Fig. 4. (a) XPS survey spectra of g-C₃N₄ and Au@g-C₃N₄, respectively, and the deconvoluted spectra of (b) C 1s, (c) N 1s, and (d) Au 4f in Au@g-C₃N₄ nanocatalyst.

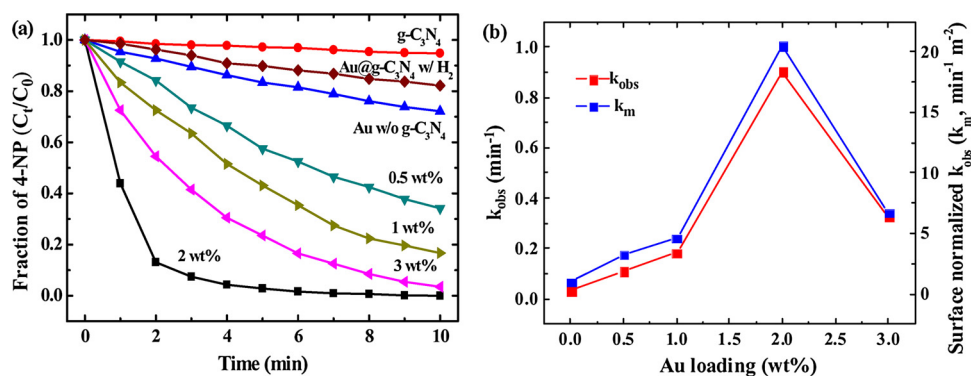


Fig. 5. (a) Effect of Au content on the reduction of 4-NP by $Au@g-C_3N_4$ and (b) the rate constant of 4-NP reduction as a function of Au loading in $Au@g-C_3N_4$ nanocatalyst in the presence of $NaBH_4$.

$NaBH_4$ is kinetically slow [3,31]. Addition of Au NPs significantly enhances the reduction efficiency and rate of 4-NP over $Au@g-C_3N_4$ in the presence of $NaBH_4$. The reduction of 4-NP to 4-aminophenol increases from 66 to > 99% when the Au loading increases from 0.5 to 2 wt%, and then slightly decreases to 96% at 3 wt% after 10 min of reaction. Only 30% of 4-NP is reduced over the Au NPs alone in the presence of $NaBH_4$, clearly indicating that the combination of Au NPs with $g-C_3N_4$ nanosheets can exhibit superior catalytic activity toward nitrophenols reduction. Only 30% of 4-NP is reduced over the Au NPs alone in the presence of $NaBH_4$, clearly indicating that the combination of Au NPs with $g-C_3N_4$ nanosheets can exhibit superior catalytic activity toward nitrophenols reduction. It is interesting to note that 18% of 4-NP is reduced over 2 wt% $Au@g-C_3N_4$ in the presence of 0.36 mL of H_2 gas (ca. 7 mM), indicating that H_2 gas, a reducing agent, can contribute to 4-NP reduction. However, the reduction efficiency and rate of 4-NP over $Au@g-C_3N_4$ in the presence of H_2 is low comparing with $NaBH_4$ due to presumably low water solubility and relatively high reduction potential.

In this study, the $NaBH_4$ concentration used is much higher than that of 4-nitrophenol and can be regarded as constant. Therefore, the effect of Au content of $Au@g-C_3N_4$ on the reduction activity can be described by the pseudo first-order kinetics (Eq. (13)). The pseudo-first-order rate constant (k_{obs}) for 4-nitrophenol reduction is 1.83×10^{-3} ($r^2 = 0.998$), 3.07×10^{-3} ($r^2 = 0.995$), 1.50×10^{-2} ($r^2 = 0.983$), and $5.33 \times 10^{-3} s^{-1}$ ($r^2 = 0.997$), respectively, over the 0.5-, 1-, 2- and 3-wt% $Au@g-C_3N_4$. When normalized to the specific surface area of $Au@g-C_3N_4$, the normalized surface rate constant (k_m) for 4-NP reduction increases from 3.24 to $20.25 min^{-1} m^{-2}$ at 0.5–2-wt% $Au@g-C_3N_4$ and then decreases to $6.78 min^{-1} m^{-2}$ at 3-wt% $Au@g-C_3N_4$. Since k_{obs} (or k_m) is a function of the product of site destiny of A and B, $k_{obs} = k_3 S_A^T S_B^T K_1 K_2 [BH_4]$, a maximum rate constant is expected at site density where both site A and site B are equal. The results indicate that 2-wt%

$Au@g-C_3N_4$ provides optimal active sites for both $NaBH_4$ and 4-NP and exhibits the best catalytic activity in comparison with other Au loadings of $Au@g-C_3N_4$ and is used for further experiments.

Generally, our rate constants are 10 times that reported by Fu et al. [23] for the reduction of p-nitrophenol by $NaBH_4$ over $Au@g-C_3N_4$; note that the rate constant reported by Fu et al. was $1.01 \times 10^{-3} s^{-1}$ over $Au@g-C_3N_4$ loaded with the same 2% Au [23]. Obviously the synthesis procedures can affect the crystal structure of the catalyst, which will impact the reactivity of the catalysts. It is noted that Fu et al. [23] prepared bulk C_3N_4 by heating 5 g of dicyandiamide into a crucible (material unknown) at $2^\circ C min^{-1}$ to $530^\circ C$ in a muffle furnace for 4 h. Our bulk C_3N_4 was prepared by heating 10 g of thiourea in a covered alumina crucible in a muffle furnace at $550^\circ C$ for 2 h at a rate of $15^\circ C min^{-1}$.

Results showed slight 4-NP reduction by hydrogen molecules (brown solid diamonds)

3.3. Reduction of different nitrophenols by $Au@g-C_3N_4$

To further understand the applicability of $Au@g-C_3N_4$ nanocomposite to catalyze the reduction of nitrophenol, several nitroaromatics including 2-NP, 3-NP, 4-NP, 2,4-DNP and 2,4,6-TNP are selected as the target compounds. As shown in Fig. 6a, the $Au@g-C_3N_4$ nanocomposite exhibits remarkable catalytic activity toward nitrophenol reduction by $NaBH_4$. Both the k_{obs} and normalized surface rate constants of nitrophenol reduction follow the order: 4-NP > 2-NP > 3-NP > 2,4-DNP > 2,4,6-TNP, indicating 4-NP reduction the most favorable over $Au@g-C_3N_4$ nanocatalyst. The rate constant of nitrophenol reduction decreases with the increase in number of nitro-substituent, which is mainly attributed to the molecular hindrance and steric effect of nitroaromatics to penetrate into the catalyst network [32–34]. Besides, the order of reactivity for nitrophenol reduction is highly

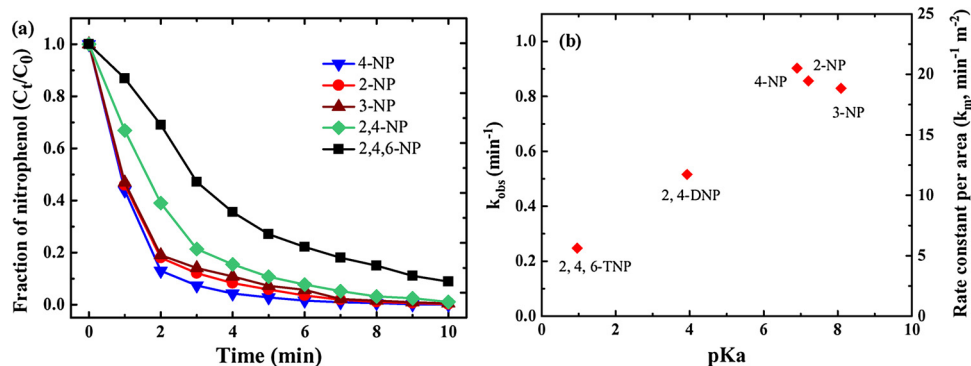


Fig. 6. (a) Catalytic reduction of various nitrophenol compounds and (b) rate constants as a function of pKa for nitroaromatic reduction by $Au@g-C_3N_4$ nanocomposite in the presence of $NaBH_4$.

dependent on the concentration (or activity) of nitrophenolate ions [35]. The acidity of nitrophenols follows the order: 2,4,6-TNP ($pK_a = 0.96$) > 2,4-DNP ($pK_a = 3.96$) > 4-NP ($pK_a = 6.90$) > 2-NP ($pK_a = 7.21$) > 3-NP ($pK_a = 8.09$).

Fig. 6b shows clearly the linear relationship between the nitrophenol reduction rate constant, k , and acidity constant, pK_a , which indicates that the activity of nitrophenolate ions plays an important role in the reduction of nitrophenols. It is noted that BH_4^- is a Lewis base, which reacts readily with the $-N^+=O_2$ group of nitrophenols. Nitrophenols with strong acidity, i.e., 2,4,6-TNP, form reactive nitrophenolate ion and result in the high reduction rate by BH_4^- over $Au@C_3N_4$. In addition, the reduction rate of 4-NP > 2-NP > 3-NP is in good agreement with the Hammett equation. The resonance stability also plays a pivotal role in determining the reactivity of nitrophenols. The negatively charged O atoms on 4-nitrophenolate ions can be delocalized throughout the benzene ring and become more resonance-stabilized than those of 2-nitrophenolate and 3-nitrophenol ions [32]. In addition, the steric hindrance effect lowers the inductive effect of the nitro group on 2- and 3-nitrophenolate ions compared with that of 4-nitrophenolate ions. Therefore, the efficiency and rate of catalytic reduction of 4-NP is higher than those of 2-NP and 3-NP. Shin et al. synthesized silver-deposited silanized magnetite beads for the catalytic reduction of nitrophenols and found that the rate of reduction of nitrophenols follows the order: 4-NP > 2-NP > 3-NP [34], which is in good agreement with our catalytic results for $Au@g-C_3N_4$ catalyst. Since 4-NP has high reactivity compared with other nitroaromatics, 4-NP is used as the model compound for the further experiments.

3.4. Effect of 4-NP concentration on the catalytic activity of $Au@g-C_3N_4$

The effect of several parameters including initial 4-NP concentration, pH, and anion on the reduction of 4-NP is further examined. Fig. 7a shows the effect of initial 4-NP concentration on the reduction efficiency of 4-NP over $Au@g-C_3N_4$. The reduction efficiency of 4-NP at various concentrations are all higher than 90% after 10 min of reaction time. However, the reduction rate decreases with the increase in 4-NP concentration from 0.1 to 0.5 mM (or 14–70 $mg\ L^{-1}$). The k_{obs} for 4-NP reduction decreases from $1.55 \times 10^{-2}\ s^{-1}$ ($r^2 = 0.961$) at 0.1 mM 4-NP to $6.43 \times 10^{-3}\ s^{-1}$ ($r^2 = 0.985$) at 0.5 mM 4-NP (inset of Fig. 7a). Several studies have examined the reduction of 4-NP over Au-based nanomaterials [36–44]. As shown in Table S1 (Supplementary data), the k_{obs} value for 4-NP reduction by the 8-nm Au-based $Au@g-C_3N_4$ nanocomposite in this study is higher than or comparable to those reported data in most previous studies [35–43], showing that the $Au@g-C_3N_4$ prepared with small-sized Au seeds in this work are promising nanocatalyst for nitrophenol reduction.

The decrease in rate constant of 4-NP at high initial 4-NP

concentration is probably attributed to the limited active sites of Au NPs. Several studies have reported that the reduction of 4-NP over Au-based nanomaterials follows the surface-mediated processes where the initial rate of reaction is positively related to adsorption, and, therefore, the initial rate of 4-NP can be used to calculate the parameters of the Langmuir-Hinshelwood kinetics model [30,45].

$$r_0 = \frac{dC_R}{dt} = k_r \frac{K_a C_R}{1 + K_a C_R} \quad (15)$$

where r_0 is the initial rate for 4-NP reduction, C_R is the 4-NP concentration; k_r is the intrinsic rate constant, and K_a is the Langmuir coefficient of 4-NP. Fig. 7b shows the initial rate for 4-NP reduction as a function of initial 4-NP concentration. The initial rate of 4-NP reduction increases positively from $6.3 \times 10^{-2}\ mM\ min^{-1}$ at 0.1 mM $NaBH_4$ to $1.95 \times 10^{-1}\ mM\ min^{-1}$ at 0.5 mM 4-NP. A good linear relationship between the initial 4-NP concentration and the initial rate for 4-NP reduction is observed, which clearly shows that the reduction of 4-nitrophenol follows the Langmuir-Hinshelwood kinetics. Based on Fig. 7b, the affinity constant and the maximum initial reaction rate of $1.79\ L\ mg^{-1}$ and $6.90 \times 10^{-3}\ mM\ s^{-1}$, respectively, are obtained ($r^2 = 0.996$) (inset of Fig. 7b).

3.5. Effect of pH on the catalytic activity of $Au@g-C_3N_4$

Fig. 8 displays the pH effect on the catalytic reactivity of $Au@g-C_3N_4$ toward 4-NP reduction. The reduction of 4-NP over $Au@g-C_3N_4$ is highly dependent on pH value; low pH is conducive to high reduction efficiency. Although a nearly complete reduction of 4-NP can be observed within 10 min at pH 3–9, the k_{obs} for 4-NP reduction decreases upon increasing pH values. As shown in the inset of Fig. 8, the k_{obs} for 4-NP reduction is in the range of 1.41×10^{-2} – $1.92 \times 10^{-2}\ s^{-1}$ at pH 3–5 and then decreases to 7.78×10^{-3} – $1.02 \times 10^{-2}\ s^{-1}$ at pH 7–9. The high reactivity of $Au@g-C_3N_4$ at low pH value is mainly attributed to the relationship between pH_{IEP} of nanocatalysts and pK_a of 4-NP. The measured pH_{IEP} of $Au@g-C_3N_4$ is at pH 4.2 (Fig. S8, Supplementary data), which means that the surface is positively charged at $pH < 4$. Since the reduction of 4-NP over $Au@g-C_3N_4$ in the presence of $NaBH_4$ follows the Langmuir-Hinshelwood kinetics and adsorption is the first step for the reduction reaction, the negatively charged BH_4^- can be easily adsorbed onto the positively charged $Au@g-C_3N_4$ surface at low pH values, resulting in an enhanced efficiency and rate of 4-NP reduction under acidic condition. Lin and Doong [45] have reported that pH plays an important role in the reduction of 4-NP and low pH accelerates the reduction efficiency and rate of 4-NP over dumbbell-like $Au-Fe_3O_4$ heterostructures, which is in good agreement with the results obtained in this study. On the other hand, the pK_a value of 4-NP is 7.2, which means that the 4-NP would primarily present in the anionic form

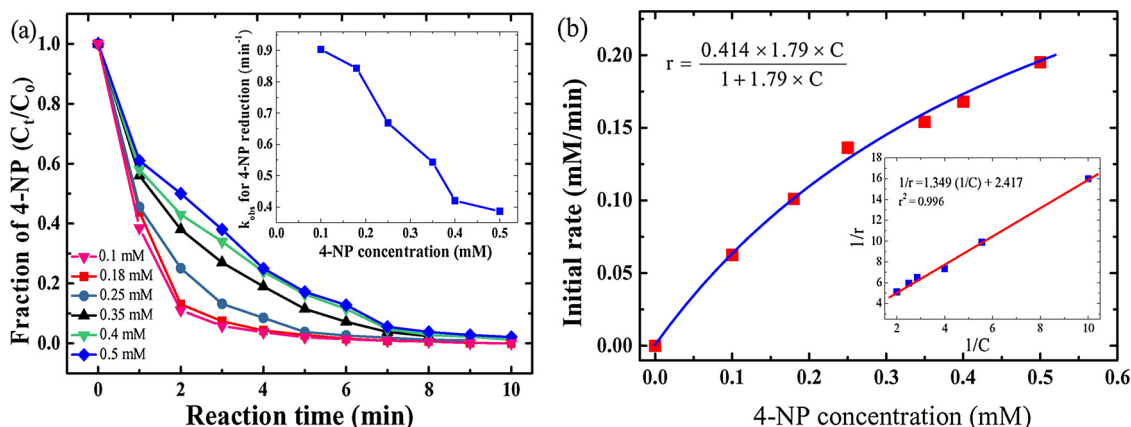


Fig. 7. (a) Reduction efficiency and (b) initial rate of 4-NP over 2 wt% $Au@g-C_3N_4$ as a function of initial 4-NP concentration at pH 5. Inset of Fig. 7a and 7b are k_{obs} of 4-NP reduction and the linear relationship of Langmuir-Hinshelwood model, respectively.

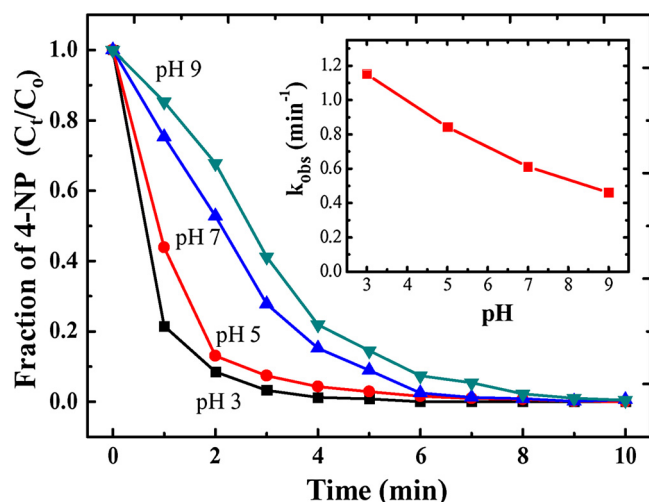


Fig. 8. Reduction efficiency and rate constant (inset) of 4-NP over 2 wt% Au@g-C₃N₄ as a function of pH ranging from 3 to 9.

when the solution pH > pK_a. Therefore, the adsorbed amount of 4-NP would be sharply decreased due to the electrostatic repulsion between 4-NP anions and the negatively charged Au@g-C₃N₄ under alkaline condition. It is also noteworthy to mention that the efficiency and rate of 4-NP reduction at various pH values is consistent with the adsorption results shown in Fig. S9 (Supplementary data), which indicates that adsorption plays an important role in determining the efficiency and rate of nitrophenols reduction over Au@g-C₃N₄.

3.6. Effect of inorganic anions on the catalytic activity of Au@g-C₃N₄

Inorganic anions usually coexist with organic pollutants in contaminated water and wastewater, and may affect the catalytic activity of Au-based catalysts. Fig. 9 shows the effect of 0.1 M anions on the reduction efficiency and rate of 4-NP over Au@g-C₃N₄ in the presence of NaBH₄. As shown in Fig. 9a, addition of dihydrogen phosphate anions (H₂PO₄[−]) significantly inhibits the reduction efficiency of 4-NP and only 70% of 4-NP is converted to 4-aminophenol after 10 min of reaction. Although a near complete conversion of 4-NP is also observed in the presence of NO₃[−], HCO₃[−] and SO₄^{2−}, the reaction rate decreases obviously when compared to that of 4-NP in the absence of anion. As shown in Fig. 9b, the k_{obs} of 4-NP reduction decreases from $1.50 \times 10^{-2} \text{ s}^{-1}$ in the absence of anion to 1.2×10^{-2} , 4.17×10^{-3} , 1.83×10^{-3} and $1.67 \times 10^{-3} \text{ s}^{-1}$ in the presence of SO₄^{2−}, HCO₃[−], NO₃[−], and H₂PO₄[−], respectively. It is interesting to note that Cl[−] can accelerate the reduction efficiency and rate of 4-NP over Au@g-C₃N₄ and the k_{obs} for 4-NP reduction is 1.11 s^{-1} . Intuitively, anions with large size or high valence easily exist in the vicinity of nanocatalyst surface because of the weaker electrostatic repulsion forces [46], which may retard the adsorption

of nitrophenolate on the catalyst surface and decrease the efficiency and rate of 4-NP reduction in the presence of anionic species. To verify the above hypothesis, we performed the adsorption experiment of 4-NP onto the Au@g-C₃N₄ in the presence of different anions without the addition of NaBH₄. Results shown in Fig. S10 (Supplementary data) indicates that the adsorption of nitrophenols onto Au@g-C₃N₄ follow the order: Cl[−] > blank > SO₄^{2−} > HCO₃[−] > NO₃[−] > H₂PO₄[−], which is in good agreement with our catalytic results for Au@g-C₃N₄ catalyst.

3.7. Stability and reusability of Au@g-C₃N₄

The stability and reusability must be considered when evaluating the engineering applications of catalysts. In this study, the stability and reusability of Au@g-C₃N₄ are examined in 10 repeated injections of 0.18 mM (or 25 mg L^{−1}) 4-NP each into the solution at pH 5.0. It is apparent that a nearly complete reduction of 4-NP over Au@g-C₃N₄ can be rapidly achieved in 10 min after 10 cycles of continuous usage (Fig. 10a). The reaction rate of 4-NP is almost the same during the first 7 cycles and then decreases slightly from $8.40 \times 10^{-1} \text{ s}^{-1}$ at the 7th cycle to $6.00 \times 10^{-1} \text{ s}^{-1}$ at the 10th cycle (Fig. 10b). The XRD patterns of Au@g-C₃N₄ after recycling of 10 times still show the clear two g-C₃N₄ peaks at 13.2° and 27.5° 2θ and one fcc Au peak at 2θ of 38.2° (Fig. S11, Supplementary data), which is similar to that of the virgin Au@g-C₃N₄. The slight decrease in k_{obs} may be attributed to the accumulation of 4-aminophenol at the active Au sites of Au@g-C₃N₄ nanocatalyst [30]. The results clearly indicate that Au@g-C₃N₄ nanocomposite is structurally stable with high catalysis efficiency and recyclability.

3.8. Possible reaction mechanism for 4-NP reduction

To gain insights into the reaction mechanism, EPR experiment is conducted at room temperature using DMPO as the spin trapper. As shown in Fig. S12 (Supplementary data), a high intensity of nine-line SPR spectrum in the field of 3460–3540 G is observed when DMPO is added to the solution containing 4-NP, NaBH₄, and Au@g-C₃N₄ (Fig. S12a). The obtained spectrum consists of a 1:1:1 triplet of 1:2:1 triplets with $a_N = 16.6 \text{ G}$ and $a_H = 22.5 \text{ G}$, which indicates the generation of large amount of H[•] radical adducts [46,47]. The H[•] radical adducts also can be produced in solution containing NaBH₄ and DMPO (Fig. S12b and c), suggesting that the H[•] radical adducts are mainly derived from NaBH₄. However, the intensity of H[•] radical adducts is low in comparison with the solution containing Au@g-C₃N₄. Besides, results of control experiments reveal that no H[•] adduct is observed for 4-NP or Au@g-C₃N₄ with and without DMPO (Fig. S12d–h). Results clearly indicate that the existence of Au@g-C₃N₄ can promote the formation of H[•] radicals over Au–H bonds in the solution. Since the catalytic reaction takes place on the Au site of Au@g-C₃N₄, the formation of the hydrogen spin adducts most likely come from the abstraction of hydrogen from the Au by a spin trap.

When Au@g-C₃N₄ nanocatalyst is used for the catalytic reduction of

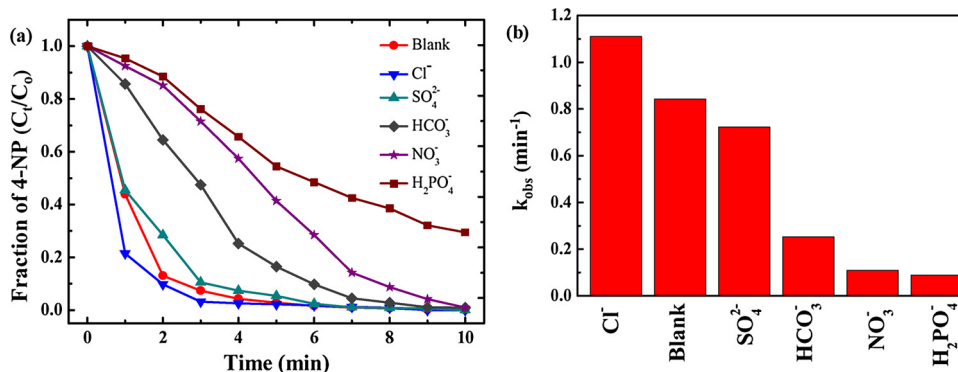


Fig. 9. Effect of inorganic anions on the catalytic reduction of 4-NP by Au@g-C₃N₄ nanocomposite and (b) pseudo-first-order rate constant.

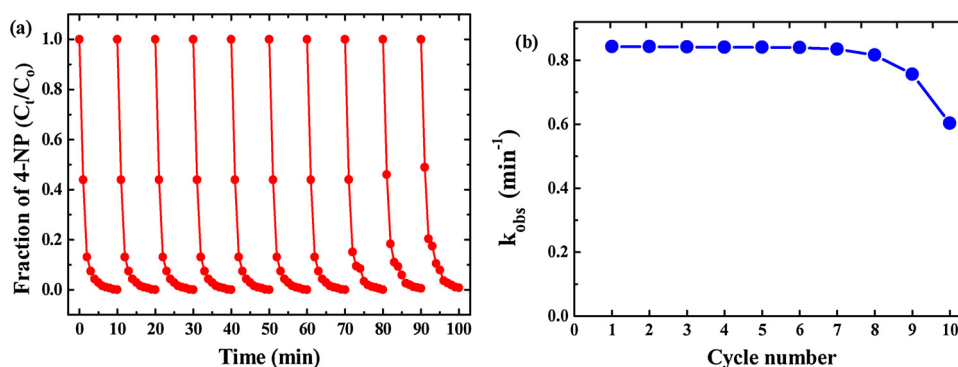
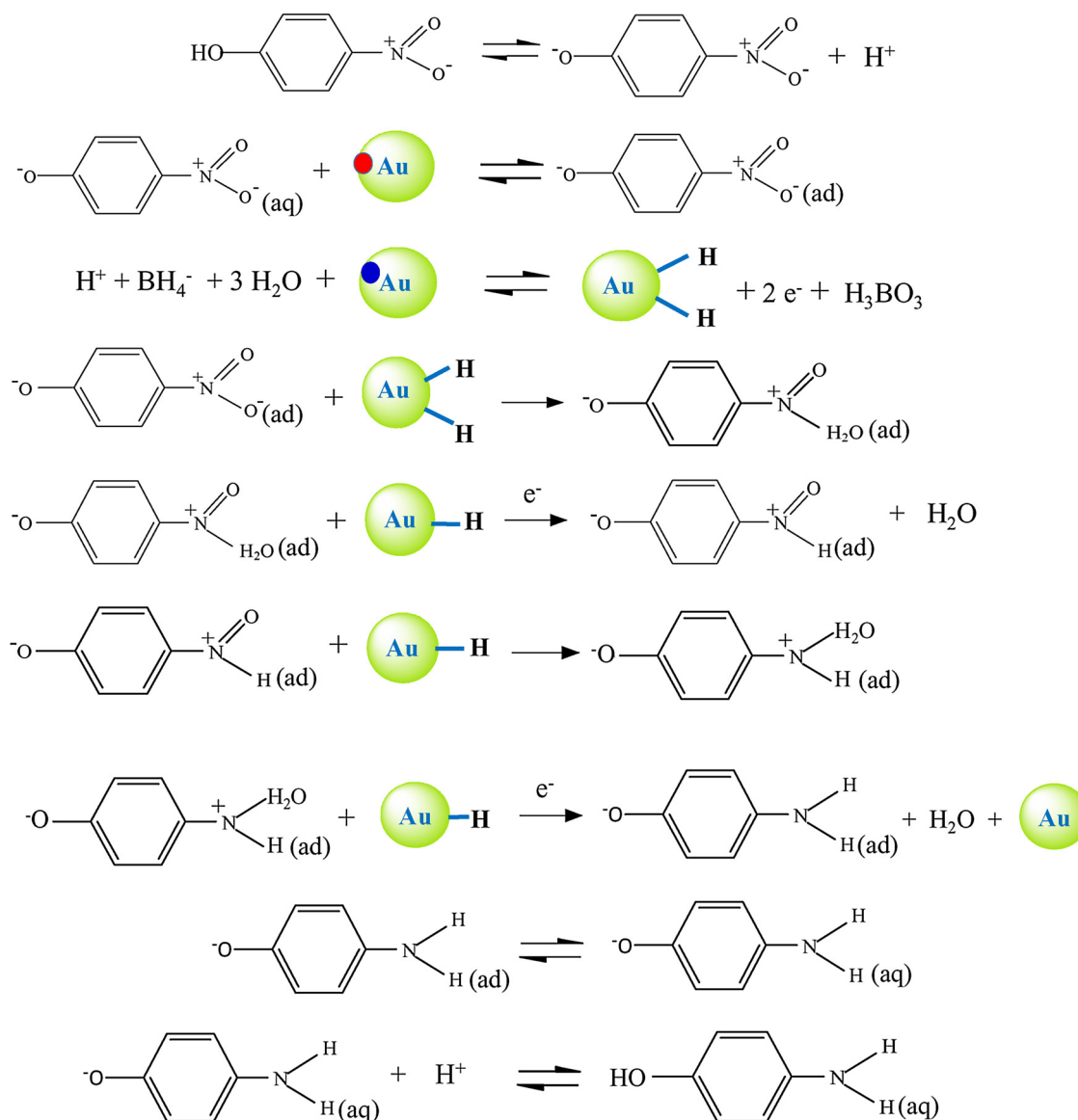


Fig. 10. The (a) recyclability and (b) reaction rate constant for the reduction of 4-NP catalyzed by the as-prepared Au@g-C₃N₄ catalyst.



Scheme 2. Proposed possible reaction pathway for the 4-NP reduction by NaBH₄ over Au@g-C₃N₄.

nitrophenols, BH₄⁻ ions are first adsorbed onto Au@g-C₃N₄ and then diffused to the Au site to form Au-H complex. The adsorption of 4-NP onto the Au@g-C₃N₄ shown in Fig. S13 (Supplementary data) is higher than that of pure Au NPs, showing that the g-C₃N₄ sheets provide large surface area for 4-NP adsorption via π - π stacking interaction [22]. As a consequence, high 4-NP concentration is accumulated on the Au@g-

C₃N₄ surface, and the porous and conductive g-C₃N₄ can transfer electrons and H[•] radicals from the adsorbed BH₄⁻ (Au-H species) to 4-NP through the catalytic Au NPs more readily, resulting in the production of 4-aminophenol. Furthermore, the porous structure of Au@g-C₃N₄ composite renders all active sites readily accessible that can significantly facilitate the rapid transport and diffusion of H[•] radicals and

electrons, resulting in the enhanced catalytic reduction on 4-NP. This process is similar to the formation of Au–H species during the alcohol oxidation [47], suggesting the formation of Au–H species and their involvement with 4-NP reduction. According to these results, a direct hydrogenation route for 4-NP catalyzed by Au@g-C₃N₄ in the presence of NaBH₄ is schematically proposed in Scheme 2.

4. Conclusions

In this study, we have developed a simple and facile synthesis method for the fabrication of Au@g-C₃N₄ nanocomposite with various Au loadings, highly recyclable, for the reduction of 4-NP. Au NPs with an average diameter of 5–15 nm are well-deposited onto the surface of g-C₃N₄ in 3–6 layers structure. The as-prepared Au@g-C₃N₄ nanocomposite exhibits good catalytic properties for nitrophenol reduction in the presence of NaBH₄ and the reaction rate follows the order: 4-NP > 2-NP > 3-NP > 2,4-DNP > 2,4,6-TNP. Furthermore, the 4-NP reduction efficiency and rate is highly dependent on environmental parameters, including pH, Au loading, NaBH₄ concentration, and foreign anions. The k_{obs} for 4-NP reduction over 2 wt% Au@g-C₃N₄ can be up to $1.50 \times 10^{-2} \text{ s}^{-1}$ in the presence of 7 mM NaBH₄ at pH 5. Although the presence of anions including H₂PO₄⁻, SO₄²⁻, HCO₃⁻ and NO₃⁻ lowers the 4-NP reaction rate, the addition of Cl⁻ ions enhances the k_{obs} by 20%. In addition, the Au@g-C₃N₄ nanocatalyst can be reused for at least 10 consecutive catalytic cycles without considerable loss in catalytic activity, indicating that the combination of low mass of Au NPs and g-C₃N₄ is a reliable green chemistry with great potential applications for catalytic transformation in the field of environmental remediation.

Acknowledgements

The authors wish to thank the Ministry of Science and Technology (MOST), Taiwan, for generous financial support under grant No. 104-2221-E-009-020-MY3 and 106-3114-E-009-012.

Appendix A. Supplementary data

Supplementary material related to this article can be found, in the online version, at doi:<https://doi.org/10.1016/j.apcatb.2018.08.035>.

References

- [1] J.G. Li, T.T. Zhao, T.K. Chen, Y.B. Liu, C.N. Ong, J.P. Xie, *Nanoscale* 7 (2015) 7502–7519.
- [2] K. Saha, S.S. Agasti, C. Kim, X. Li, V.M. Rotello, *Chem. Rev.* 112 (2012) 2739–2779.
- [3] M.N. Nadagouda, T.F. Speth, R.S. Varma, *Acc. Chem. Res.* 44 (2011) 469–478.
- [4] C.J. Jia, Y. Liu, H. Bongard, F. Schuth, *J. Am. Chem. Soc.* 132 (2010) 1520–1527.
- [5] F.H. Lin, R.A. Doong, *J. Phys. Chem. C* 121 (2017) 7844–7853.
- [6] S.A. Shahzad, M.A. Sajid, Z.A. Khan, D. Canseco-Gonzalez, *Synth. Commun.* 47 (2017) 735–755.
- [7] T. Bhowmik, M.K. Kundu, S. Barman, *RSC Adv.* 5 (2015) 38760–38773.
- [8] N. Pradhan, A. Pal, T. Pal, *Langmuir* (2001) 1800–1802.
- [9] M.K. Corbierre, N.S. Cameron, M. Sutton, K. Laaziri, R.B. Lennox, *Langmuir* 21 (2005) 6063–6072.
- [10] R. Torres-Mendieta, D. Ventura-Espinosa, S. Sabater, J. Lancis, G. Minguez-Vega, J.A. Mata, *Sci. Rep.* 6 (2016) 30478.
- [11] A. Dhakshinamoorthy, A.M. Asiri, H. Garcia, *ACS Catal.* 7 (2017) 2896–2919.
- [12] C. Tan, X. Cao, X.J. Wu, Q. He, J. Yang, X. Zhang, J. Chen, W. Zhao, S. Han, G.H. Nam, M. Sindoro, *Chem. Rev.* 117 (2017) 6225–6331.
- [13] W.J. Ong, L.L. Tan, Y.H. Ng, S.T. Yong, S.P. Chai, *Chem. Rev.* 116 (2016) 7159–7329.
- [14] I. Majeed, U. Manzoor, F.K. Kanodarwala, M.A. Nadeem, E. Hussain, H. Ali, A. Badshah, J.A. Stride, M.A. Nadeem, *Catal. Sci. Technol.* 8 (2018) 1183–1193.
- [15] M. Caux, F. Fina, J.T.S. Irvine, H. Idriss, R. Howe, *Catal. Today* 287 (2017) 182–188.
- [16] S. Verma, R.B. Nasir Baig, M.N. Nadgouda, R.S. Varma, *ACS Sustain. Chem. Eng.* 5 (2017) 3637–3640.
- [17] J.H. Lee, M.J. Park, S.J. Yoo, J.H. Jang, H.J. Kim, S.W. Nam, C.W. Yoon, J.Y. Kim, *Nanoscale* 7 (2015) 10334–10339.
- [18] S.K. Konda, M. Amiri, A. Chen, *J. Phys. Chem. C* 120 (2016) 14467–14473.
- [19] G. Mamba, A.K. Mishra, *Appl. Catal. B Environ.* 198 (2016) 347–377.
- [20] R.C. Pawar, Y. Pyo, S.H. Ahn, C.S. Lee, *Appl. Catal. B Environ.* 176 (2015) 654–666.
- [21] V.K. Tomer, N. Thangaraj, S. Gahlot, K. Kailasam, *Nanoscale* 8 (2016) 19794–19803.
- [22] X.G. Cai, J.Y. He, L. Chen, K. Chen, Y.L. Li, K.S. Zhang, Z. Jin, J.Y. Liu, C.M. Wang, X.G. Wang, L.T. Kong, J.H. Liu, *Chemosphere* 171 (2017) 192–201.
- [23] M. Fu, T. Huang, B. Jia, J. Zhu, X. Wang, *Appl. Catal. B* 202 (2017) 430–437.
- [24] J. Xu, T.J. Brenner, Z. Chen, D. Neher, M. Antonietti, M. Shalom, *ACS Appl. Mater. Interfaces* 6 (2014) 16481–16486.
- [25] J. Barrio, L. Lin, X. Wang, M. Shalom, *ACS Sustain. Chem. Eng.* 6 (2018) 519–530.
- [26] M. Chaudhary, R.A. Doong, N. Kuman, T.Y. Tseng, *Appl. Surf. Sci.* 420 (2017) 118–128.
- [27] S. Samanta, R. Srivastava, *Appl. Catal. B Environ.* 218 (2017) 621–636.
- [28] Y. Kofuji, S. Ohkita, Y. Shiraishi, H. Sakamoto, S. Tanaka, S. Ichikawa, T. Hirai, *ACS Catal.* 6 (2016) 7021–7029.
- [29] K.C. O'Connell, J.R. Monnier, J.R. Regalbuto, *Appl. Catal. B Environ.* 225 (2018) 264–272.
- [30] F.H. Lin, R.A. Doong, *J. Phys. Chem. C* 115 (2011) 6591–6598.
- [31] S. Saha, A. Pal, S. Kundu, S. Basu, T. Pal, *Langmuir* 26 (2009) 2885–2893.
- [32] S. Jana, S.K. Ghosh, S. Nath, S. Pande, S. Praharaj, S. Panigrahi, S. Basu, T. Endo, T. Pal, *Appl. Catal. A Gen.* 313 (2006) 41–48.
- [33] K.S. Shin, Y.K. Cho, J.Y. Choi, K. Kim, *Appl. Catal. A Gen.* 413 (2012) 170–175.
- [34] V.K. Gupta, N. Atar, M.L. Yola, Z. Ustundag, L. Uzun, *Water Res.* 48 (2014) 210–217.
- [35] A. Goyal, S. Bansal, V. Kumar, J. Singh, S. Singhal, *Appl. Surf. Sci.* 324 (2015) 877–889.
- [36] Y.Y. Ju, X. Li, J. Feng, Y.H. Ma, J. Hu, X.G. Chen, *Appl. Surf. Sci.* 316 (2014) 132–140.
- [37] Y.W. Yang, Y.Y. Mao, B. Wang, X.W. Meng, J. Han, C. Wang, H.W. Yang, *RSC Adv.* 6 (2016) 32430–32433.
- [38] T. Zeng, X.L. Zhang, S.H. Wang, Y.R. Ma, H.Y. Niu, Y.Q. Cai, *J. Mater. Chem. A Mater. Energy Sustain.* 1 (2013) 11641–11647.
- [39] Y.Z. Ni, G.S. Tong, J. Wang, H.M. Li, F. Chen, C.Y. Yu, Y.F. Zhou, *RSC Adv.* 6 (2016) 40698–40705.
- [40] Z. Chen, Z.M. Cui, C.Y. Cao, W.D. He, L. Jiang, W.G. Song, *Langmuir* 28 (2012) 13452–13458.
- [41] W.C. Guo, Q. Wang, Y. Luan, G. Wang, W.J. Dong, J. Yu, *Chem. Asian J.* 10 (2015) 701–708.
- [42] Y.H. Zhu, J.H. Shen, K.F. Zhou, C. Chen, X.L. Yang, C.Z. Li, *J. Phys. Chem. C* 115 (2011) 1614–1619.
- [43] Y.H. Deng, Y. Cai, Z.K. Sun, J. Liu, C. Liu, J. Wei, W. Li, C. Liu, Y. Wang, D.Y. Zhao, *J. Am. Chem. Soc.* 132 (2010) 8466–8473.
- [44] J. Li, C.Y. Liu, Y. Liu, *J. Mater. Chem.* 22 (2012) 8426–8430.
- [45] F.H. Lin, R.A. Doong, *Appl. Catal. A Gen.* 486 (2014) 32–41.
- [46] T. Aditya, J. Jana, N.K. Singh, A. Pal, T. Pal, *ACS Omega* 2 (2017) 1968–1984.
- [47] M. Conte, H. Miyamura, S. Kobayashi, V. Chechik, *J. Am. Chem. Soc.* 131 (2009) 7189–7196.